LASER & PHOTONICS REVIEWS
www.lpr-journal.org

Polarization-Independent Complex Bragg Grating Filters on Silicon Nitride

Alejandro Fernández-Hinestrosa, José Manuel Luque-González, Pavel Cheben, Jens H. Schmid, Alejandro Sánchez-Postigo, J. Gonzalo Wangüemert-Pérez, Iñigo Molina-Fernández, and Alejandro Ortega-Moñux*

Integrated optical filters are essential components of on-chip multiplexers, which play a critical role in enhancing data throughput for high-demand networks. Since optical multiplexers are typically connected through fiber-optic links where the polarization state of light fluctuates randomly, polarization insensitivity is an important prerequisite for integrated optical filters. In this work, polarization-insensitive optical filters are demonstrated on the silicon nitride platform operating in the datacom O-band. The filters are based on cladding-modulated Bragg gratings, which offer improved fabrication tolerances and reduced losses compared to conventional sidewall gratings. By judiciously designing grating dimensions, filters are demonstrated with single-band, dual-band, and four-band spectral characteristics. The fabricated filters achieve an insertion loss below 1.0 dB and a band rejection greater than 25 dB for spectral bands that are 3 nm wide and 9 nm apart.

1. Introduction

Silicon photonics has become established as a reliable technology for highly integrated optical components.[1,2] Both silicon-on-insulator (SOI) and silicon nitride platforms are compatible with mature CMOS microelectronics, reducing manufacturing costs and enabling large-scale production of photonic integrated circuits. Recently, optical systems based on silicon nitride have gained popularity due to their high tolerance to fabrication errors and their low loss,[3,4] which benefit applications such as quantum photonics,[5] biochemical sensing,[6] and wavelength division multiplexing (WDM).[7,8] In the context of WDM, significant efforts have focused on developing high-performance integrated multiplexers for high-capacity fiber-optic links in data centers.[9] In these links, polarization diversity schemes, which remain a common solution for long-haul optical networks, are generally avoided due to their associated complexity and costs. Moreover, such schemes require dedicated components such as polarization beam splitters (PBS) and rotators (PR), which, in practice, increase power loss and demand larger footprints.[10–14] In passive optical networks (PON) and data centers, polarization-insensitive receivers are highly preferred, as they can handle any arbitrary polarization state of light coming from the output of fiber-optical cables without the need for on-chip dedicated polarization management. This preference has driven extensive research into polarization-independent integrated optical components in recent years.[11–18]

WDM multiplexers typically utilize arrayed waveguide gratings or fiber Bragg gratings operating with minimal loss and crosstalk. Conventional waveguide Bragg gratings comprise a waveguide core with a periodic perturbation that creates a photonic bandgap, thereby forbidding light propagation and reflecting it within specific wavelength ranges. An integrated solution for wavelength multiplexers relies on incorporating a pair of identical waveguide Bragg gratings into the arms of a Mach-Zehnder interferometer (MZI).[19–22] By spectrally tailoring these Bragg gratings, the wavelength multiplexer can exhibit flat-top frequency responses of several bands.[23,24] To reach the polarization-agnostic operation, both the gratings and beam splitters of the MZI must also be insensitive to polarization. Integrated beam splitters are often realized using multi-mode interference (MMI) devices, which have been extensively studied in the literature and feature accessible design procedures for achieving polarization insensitivity.[25,26] In contrast, the design of polarization-insensitive Bragg gratings has not been largely researched. By imprinting both side-

A. Fernández-Hinestrosa, J. M. Luque-González, A. Sánchez-Postigo, J. G. Wangüemert-Pérez, I. Molina-Fernández, A. Ortega-Moñux
Photonics and RF Research Lab
Telecommunication Research Institute (TELMA)
Universidad de Málaga
Bulevar Louis Pasteur 35, Málaga 29010, Spain
E-mail: afhinestrosa@uma.es

P. Cheben, J. H. Schmid
National Research Council Canada
1200 Montreal Road, Bldg. M50, Ottawa K1A 0R6, Canada

The ORCID identification number(s) for the author(s) of this article can be found under https://doi.org/10.1002/lpor.202402114

DOI: 10.1002/lpor.202402114

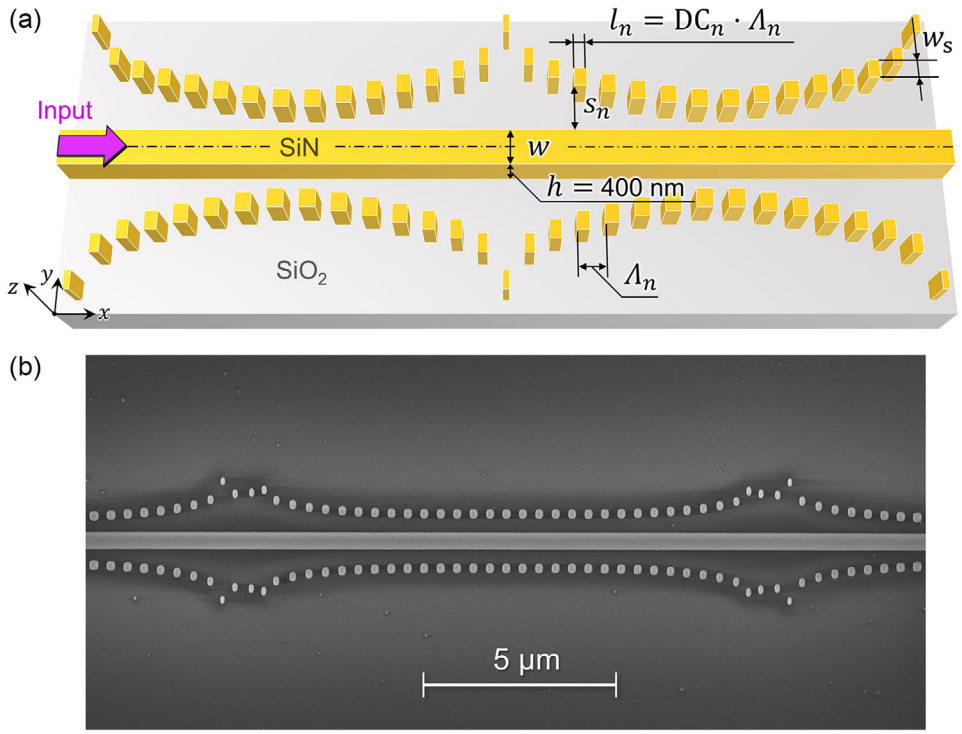

Figure 1. a) Schematic 3D view of a polarization-insensitive cladding-modulated Bragg grating. b) Scanning electron microscope (SEM) image of a section of a multi-band polarization-insensitive Bragg filter fabricated on a 400-nm thick silicon nitride platform.

wall and surface corrugations on a waveguide, polarization-insensitive Bragg gratings have been demonstrated in SOI and silicon nitride platforms.[18,27–29] Alternatively, polarization independence has been achieved by combining two Bragg gratings that separately process TE and TM modes.[30] Still, none of these approaches provides multi-band spectral characteristics, which is a critical feature for add-drop multiplexing applications.

Bragg gratings with multi-band rejection can be achieved by a precise modulation of the sidewall corrugation,[31,32] but this complicates fabrication and limits the degrees of freedom available to achieve polarization insensitivity. Our cladding-modulated Bragg gratings, illustrated in **Figure 1**, overcome this problem by externalizing the refractive index modulation as laterally loaded grating segments.[33–35] This grating topology advantageously offers relaxed fabrication tolerances and increased design flexibility through the customizable size and position of the segments,[24] but polarization independence has not yet been demonstrated. In this work, we present cladding-modulated Bragg gratings that exhibit both flat-top multi-band spectral response and polarization insensitivity. These characteristics are achieved by judiciously modulating the separation (s_n) and length (l_n) of the loading segments, resulting in a complex cladding-modulated grating. This new design strategy is experimentally validated by implementing a set of waveguide filters with single-band, dual-band, and four-band rejection spectra, complying with the LAN-WDM frequency grid,[36,37] on a 400-nm thick silicon nitride platform. Our results constitute the first demonstration of complex on-chip Bragg filters with polarization-independent performance.

2. Theory and Design

2.1. Polarization-Insensitive Uniform Bragg Filters

Waveguide Bragg gratings are periodic structures that operate as band-rejection filters. They can be analyzed via the coupled-mode theory (CMT) by dividing them into i) a waveguide with an invariant cross-section and ii) a superimposed periodic permittivity modulation with period Λ, that is, a perturbation $\Delta\epsilon(x, y, z) = \Delta\epsilon(x + \Lambda, y, z)$. A modal analysis of the waveguide determines both the field profile, $\boldsymbol{E}(y, z)$, and the effective index $n_{\text{eff}}(\lambda)$ and group index $n_g(\lambda)$ of the fundamental mode. The Bragg period is defined as:

$$\Lambda_B = \frac{\lambda_0}{2n_{\text{eff}}(\lambda_0)} \tag{1}$$

where λ_0 is the resonance wavelength for a small perturbation limit. With increasing the perturbation magnitude, the resonance wavelength shifts to $\lambda_c = \lambda_0 + \delta\lambda$, where $\delta\lambda$ depends on the mean permittivity of the periodic perturbation, $\Delta\epsilon_0(y, z)$, and the field profile of the unperturbed waveguide: $\delta\lambda \propto \int_S \Delta\epsilon_0(y, z) \cdot |\boldsymbol{E}(y, z)|^2 \, dS$. According to the coupled-mode theory, this shift is related to the self-coupling coefficient:[38]

$$\kappa' = \frac{\pi}{\Lambda_B} - \frac{2\pi\, n_{\text{eff}}(\lambda_c)}{\lambda_c} \approx \frac{\pi\, n_g(\lambda_c)}{\lambda_c^2} \cdot 2\,\delta\lambda \tag{2}$$

The fundamental mode is coupled backward within a rejection bandwidth, $\Delta\lambda$, which is a function of the interaction between

the first harmonic of the periodic perturbation, $\Delta\epsilon_1(y, z)$, and the field profile of the waveguide: $\Delta\lambda \propto \int_S \Delta\epsilon_1(y, z) \cdot |\boldsymbol{E}(y, z)|^2 \, dS$. The rejection bandwidth is related to the coupling coefficient:[38]

$$\kappa = \frac{\pi n_g(\lambda_c)}{\lambda_c^2} \cdot \Delta\lambda \tag{3}$$

A uniform Bragg grating can be insensitive to polarization when TE- and TM-polarized modes meet the following conditions:

$$n_{eff}^{TE} \cong n_{eff}^{TM}, n_g^{TE} \cong n_g^{TM}, \kappa_{TE} \cong \kappa_{TM}, \kappa'_{TE} \cong \kappa'_{TM} \tag{4}$$

To satisfy the first and second conditions, we use a square waveguide cross-section, with dimensions $w = h = 400$ nm, for which the resonance wavelengths of TE and TM modes match for a small perturbation. The grating pitch ($\Lambda_B = 430$ nm) is then calculated using Equation (1) from the effective index of the TE- and TM-polarized fundamental modes of the waveguide at $\lambda_0 = 1310$ nm. Subsequently, lateral loading segments are introduced as a periodic perturbation with a period Λ_B, located at a distance s from the waveguide. To fulfill the third and fourth terms of Equation (4), the length of the loading segments, which interact differently with the evanescent fields of the TE and TM propagating modes, is judiciously adjusted.

We begin by analyzing the uniform Bragg grating in **Figure 2**a (inset). The segment width (w_s), separation (s), and duty cycle (DC) are set to 200, 420 nm and 0.5, respectively. First, we calculate the bandgap width ($\Delta\lambda$) and the resonance wavelength (λ_c) of the structure for both TE- and TM-polarized fields using the MIT Photonics Bands (MPB) solver, as outlined in our previous work.[22] Next, we obtain the coupling (κ) and the self-coupling (κ') coefficients from Equations (3) and (2), respectively. These coefficients are then employed using the transfer-matrix method (TMM)[23,39] to calculate the TE and TM transmittances of the grating. As can be observed in Figure 2a, the notches in the TE and TM transmittance spectra differ in both resonance wavelength and rejection, indicating a polarization-dependent coupling coefficient. The coupling coefficients for both polarizations can be matched by optimizing the device geometry. Figure 2b shows that, for a duty cycle DC = 0.32, TE and TM bandgaps are equalized. Both Figure 2a,b results are calculated for a grating with $N = 1400$ periods, but the same procedure works for any arbitrary number of periods. This example suggests that for a given segment separation, s, it is possible to find an optimal duty cycle, DC, at which TE and TM transmittances practically match .

By applying the same procedure to each segment separation s in the range from 200 nm to 1 μm, we obtain the duty cycle as a function of s, DC(s), shown in Figure 2c. This function constrains the grating topology to a reduced set of solutions, where the TE and TM coupling coefficients coincide (Figure 2d). We observe a slight difference between the TE and TM self-coupling coefficients, affecting differently the central wavelengths for the two polarizations. To quantify this effect, we define the polarization wavelength detuning, $\delta\lambda_{pol}$, as the difference between the central wavelength shifts induced by the self-coupling effect for the TE and TM polarizations, i.e., $\delta\lambda_{pol} = |\delta\lambda_{TE} - \delta\lambda_{TM}|$. We calculate this detuning using Equation (2) and the κ' curves in Figure 2d. The polarization wavelength detuning is less than half a nanometer for uniform gratings with lateral segments at a separation s > 350 nm (Figure 2e). Bragg gratings with such lateral segment separation have bandgap widths ($\Delta\lambda$) less than 6 nm, as shown in Figure 2f. Furthermore, polarization wavelength detuning remains below 20% of the notch bandwidth for lateral segment width and length typical deviations of ±20 nm.

2.2. Polarization-Insensitive Multi-Band Bragg Filters

Cladding-modulated Bragg gratings are particularly well suited for multi-band filtering. By judiciously adjusting the separation, s_n, and pitch, Λ_n, of the lateral segments, an arbitrary spectral response can be synthesized.[24,22] Here we use the following general design procedure: first, from the target spectral response, we calculate the local reflection coefficient, ρ_n, for each segment n, using the layer-peeling algorithm (LPA).[23] Next, the amplitudes of the reflection coefficients are mapped to coupling coefficients, κ_n, according to the relation:

$$\kappa_n = \frac{\tanh^{-1}(|\rho_n|)}{\Lambda_B} \tag{5}$$

which is then synthesized by selecting the appropriate segment separations, s_n. The phase modulation of the reflection coefficients is obtained by tuning the period of each segment:[24]

$$\Lambda_n = \left[\frac{2\pi + \angle\rho_{n+1} - \angle\rho_n}{2\pi + 2\Lambda_B\kappa'_n}\right] \cdot \Lambda_B \tag{6}$$

where $\angle\rho_n$ is the phase of the reflection coefficient at the nth segment.

Polarization-insensitive multi-band Bragg gratings were designed on a silicon nitride waveguide with dimensions $w = h = 400$ nm, loading segments of width $w_s = 200$ nm and a nominal pitch of $\Lambda = 430$ nm. Using the layer-peeling algorithm, we obtained the reflection coefficients ρ_n for single-band, dual-band, and four-band target rejection spectra complying with the LAN-WDM standard. Rejection spectra were all centered at $\lambda_0 = 1310$ nm, with 9-nm spacing and 3-nm notch 3-dB bandwidth. Multi-band Bragg filters with twice the LAN-WDM spacing (i.e., 9 nm) enable interferometry-based add-drop interleavers[22] that drop odd bands and pass even bands (or vice versa), but the proposed design technique is valid for any band spacing greater than the rejection notch bandwidth. Using Equation (5) and the inverse of the $\kappa(s)$ function from Figure 2d, we calculated the segment separations s_n. The phase modulation of the reflection coefficients was mapped to the grating period using Equation (6) and the average function

$$\kappa'(s) = \left[\kappa'_{TE}(s) + \kappa'_{TM}(s)\right]/2 \tag{7}$$

from Figure 2d. This procedure recentered the TE and TM resonance wavelengths of each period at $\lambda_0 = 1310$ nm. To enforce polarization independence, we adjusted the segment length of each period, $l_n = DC(s_n) \cdot \Lambda_n$, using the optimized function DC(s) shown in Figure 2c. The resulting geometrical parameters are shown in **Figure 3**a–c. The filter length was chosen as 600 μm (i.e., $N = 1400$ periods) to achieve notch rejection, R, exceeding

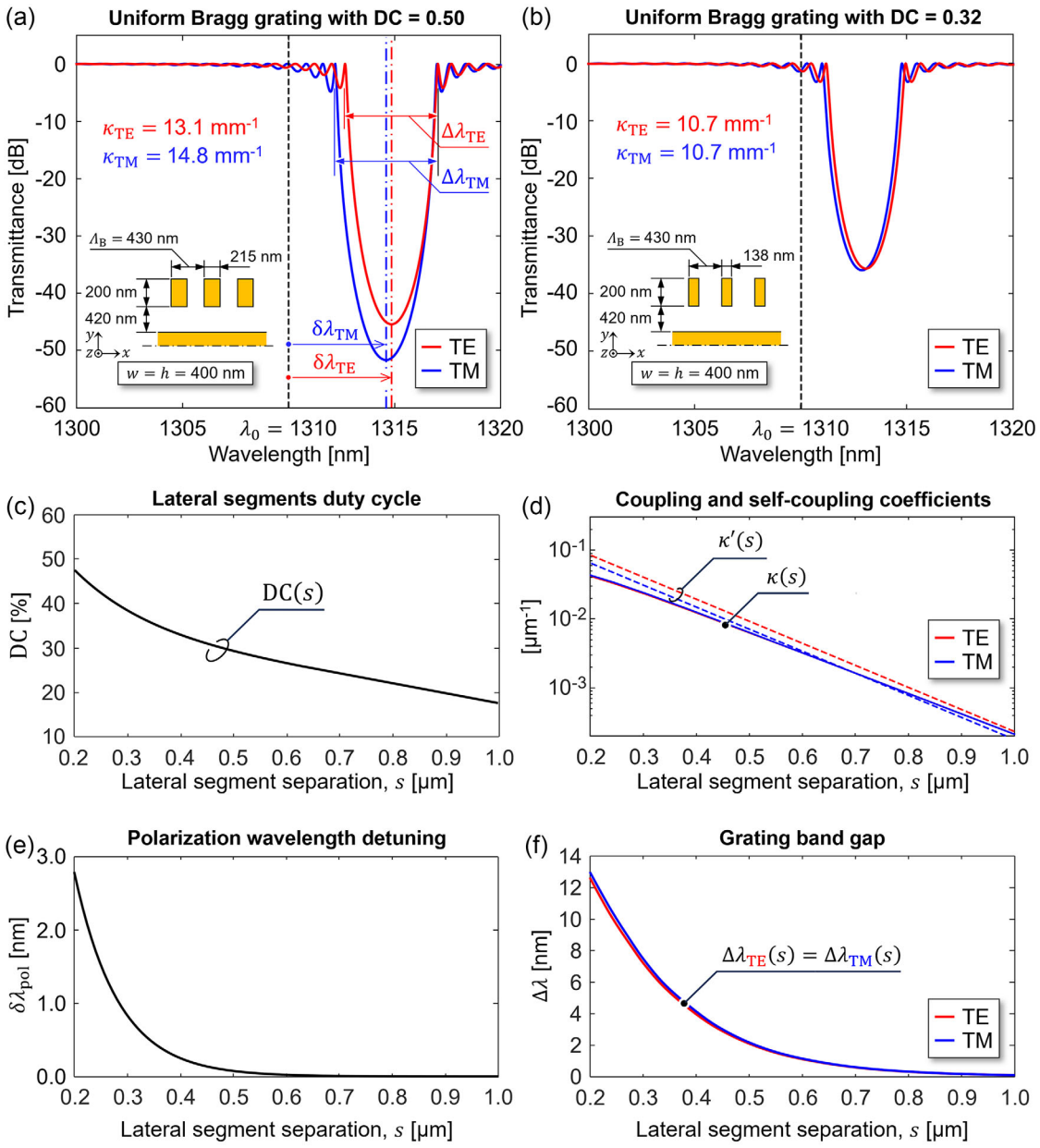

Figure 2. Uniform cladding-modulated Bragg gratings for lateral segment duty cycles of a) DC = 0.5, and b) DC = 0.32. Both gratings consist of N = 1400 periods, and the grating dimensions are shown in the insets. c) Grating duty cycle as a function of segment separation, DC(s), resulting in matched TE and TM bandgaps. d) Coupling (κ) and self-coupling (κ') coefficients for the bandwidth-matched (i.e., κ-matched) cladding-modulated Bragg grating. e) Polarization wavelength detuning as a function of segment separation, $\delta\lambda_{pol}(s)$, which is defined as the difference between the central wavelength shifts induced by the self-coupling effect for the TE and TM polarizations. f) TE and TM bandgap width of the polarization-insensitive grating as a function of segment separation.

20 dB. The simulated grating spectra, obtained by the transfer-matrix method, are presented in Figure 3d–f. It is observed that the filters are practically polarization-insensitive, with TE and TM central wavelengths differing by less than 300 pm in the worst-case scenario (Figure 3f).

The histograms in Figure 3g–i show the relative frequency (green bins) of the lateral segment separations for the gratings in Figure 3a–c, respectively. Also displayed for reference is the simulated polarization detuning (black lines) of the uniform cladding-modulated Bragg grating as a function of segment separation. For the single-band filter (Figure 3a), the polarization detuning is very small compared to the filter bandwidth, as most segments lie within a range that contributes minimally to polarization wavelength detuning (Figure 3g). As the number of rejection bands increases, the segments are localized closer to the waveguide but become more dispersed, due to an increased fluctuation of the reflection coefficients. Both of these effects contribute only to a slight detuning between the TE and TM filter

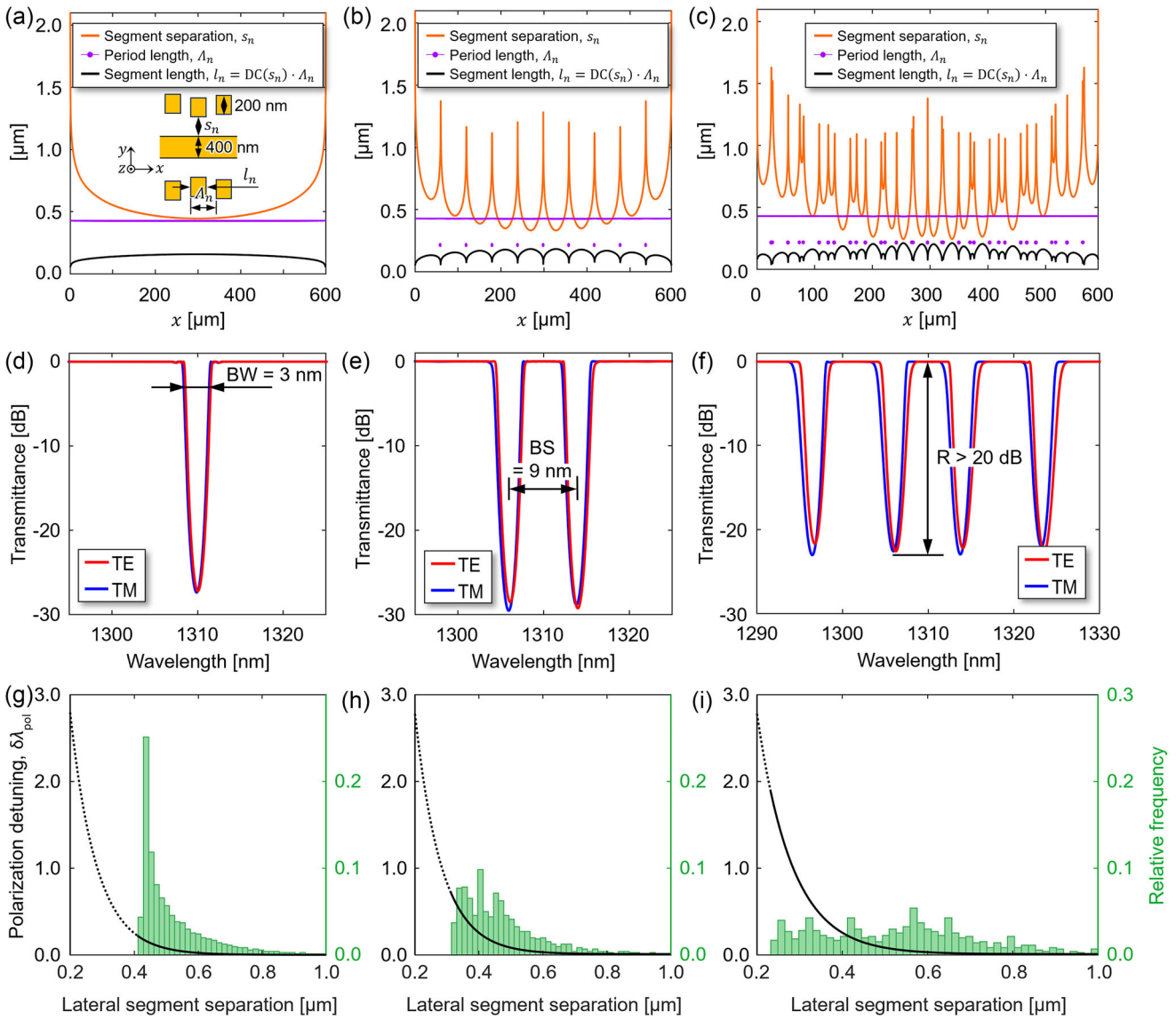

Figure 3. Geometric parameters of the polarization-insensitive cladding-modulated Bragg gratings along the grating length (x), for a) single-band, b) dual-band, and c) four-band spectra, with the corresponding transmittances d–f). Polarization wavelength detuning of the uniform grating (black curves) and relative frequency distribution of the segment separations (green bins) for: g) the single-band, h) the dual-band, and i) the four-band cladding-modulated Bragg gratings. Segments closer to the waveguide core contribute more significantly to total polarization wavelength detuning. As the number of rejection bands increases from g) to i), the minimum segment separation decreases, but the segments also spread more widely.

spectra, which becomes barely noticeable in filters with four or more rejection bands. The polarization wavelength detuning in these multi-notch filters can be estimated numerically using the following expression:

$$\delta\lambda_{\mathrm{pol}} = \frac{\sum_n \left|\lambda_{c,n}^{\mathrm{TE}} - \lambda_{c,n}^{\mathrm{TM}}\right| \cdot |\rho_n|^2}{\sum_n |\rho_n|^2} \tag{8}$$

where λ_n^{TE} and λ_n^{TM} are the TE and TM resonance wavelengths at period n. Using this equation, we estimated polarization wavelength detunings of 125, 180, and 300 pm for the single-band, dual-band, and four-band notch filters, respectively, matching closely the results shown in Figure 3d–f.

3. Experimental Results

Polarization-insensitive single-band, dual-band, and four-band rejection filters were fabricated on a conventional 400-nm-thick silicon nitride platform, provided by Applied Nanotools,[40] with a 4.5-μm-thick buried oxide layer and 3-μm-thick silicon dioxide cladding. The material refractive indices at the operating wavelength (λ_0 = 1310 nm) are n_{SiN} = 2.001 and $n_{\mathrm{SiO_2}}$ = 1.447. The structures were patterned using electron-beam lithography and anisotropic ICP-RIE etching. To compensate for etching devia-

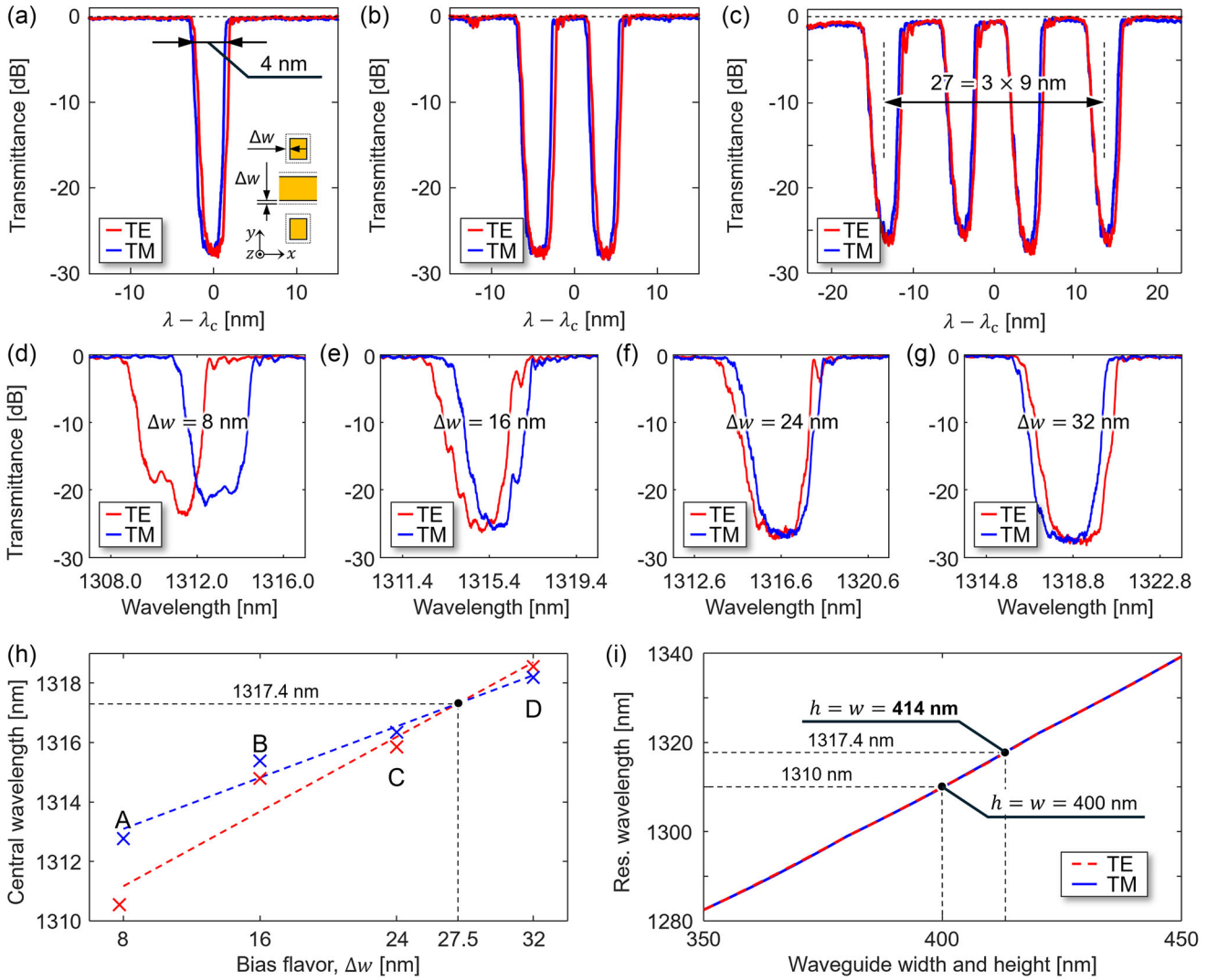

Figure 4. Experimental transmittances of the polarization-insensitive cladding-modulated Bragg filters with a bias of $\Delta w = 32$ nm for: a) one rejection band, b) two rejection bands, and c) four rejection bands. The central wavelength for all transmittances is $\lambda_c = 1318.2$ nm. Measured TE and TM transmittances of fabricated single-band filters with biases of: d) $\Delta w = 8$ nm, e) $\Delta w = 16$ nm, f) $\Delta w = 24$ nm, and g) $\Delta w = 32$ nm. h) Least squares approximation (dashed lines) of the resonance wavelengths of TE and TM polarized modes of the fabricated single-band filters (markers). A polarization-insensitive filter with a bias of $\Delta w = 27.5$ nm is estimated to resonate at 1317.4 nm. i) Simulated resonance wavelength of a single-band cladding-modulated Bragg grating with a square cross-section waveguide as a function of waveguide width and height, $w = h$. A grating with a waveguide of $w = h = 414$ nm resonates at 1317.4 nm.

tions in the fabrication process, we included several variations of our designs with respect to the bias, Δw, defined in the inset of **Figure** 4a. Positive bias values indicate an underetch (i.e., where the silicon nitride removal is less than expected), while negative values correspond to an overetch. For the experimental measurements, light from a tunable laser source (Agilent 81672B) was coupled to a half-wave plate polarization controller via a polarization-maintaining optical fiber. The light was injected into the chip facet using a lensed optical fiber and an on-chip edge coupler, and was subsequently guided to the filters through single-mode strip waveguides. Finally, the output light was collected by a microscope objective and detected using a lightwave multimeter (Agilent 81642B). All optical measurements were referenced to the transmittance of the closest straight waveguide.

Polarization insensitivity was effectively achieved for the fabricated filters with biases of $\Delta w = 24$ nm and $\Delta w = 32$ nm. Figure 4a–c shows the experimentally measured spectra of the single-band, two-band, and four-band filters for $\Delta w = 32$ nm. These spectra are in excellent agreement with simulation results in terms of shape, band spacing (9 nm), insertion loss (<1 dB), and rejection (>25 dB). The notches are ~ 1 nm wider than expected, which we attribute to increased field interaction with the larger loading segments. These results clearly validate the proposed concept and our design methodology.

Finally, we conducted an analysis to assess the impact of fabrication deviations. Figure 4d–g shows the experimentally measured optical transmittances of single-band filters with biases Δw of 8, 16, 24, and 32 nm, respectively. As Δw increases, the TE

and TM rejection bands shift in opposite directions, suggesting that a bias between 24 and 32 nm would provide perfect polarization insensitivity. Using the least squares method, we linearly approximated the measured TE and TM central wavelengths, as shown in Figure 4h. Based on this analysis, we estimated that a fabricated filter with a bias of $\Delta w = 27.5$ nm would resonate at a wavelength of 1317.4 nm for both polarizations. Next, we simulated the resonance wavelength of a single-band polarization-insensitive filter as a function of the waveguide width and height ($w = h$) (Figure 4i). From this simulation, it was apparent that a grating with a waveguide core cross-section of 414 × 414 nm would also resonate at a wavelength of 1317.4 nm for both polarizations. This result indicated a thickness error of $\Delta h = 414 - 400 = 14$ nm in the silicon nitride layer, and an actual waveguide width overetch of $\Delta w' = 427.5 - 414 = 14.5$ nm, both of which are within the typical fabrication deviation specifications of the foundry.

4. Conclusion

We have demonstrated, to the best of our knowledge, the first on-chip multi-band polarization-insensitive Bragg filters. The filters are based on cladding-modulated Bragg gratings, where the fundamental mode of a strip waveguide is evanescently coupled to loading segments, which synthesize complex amplitude and phase modulation. Furthermore, we developed a novel design methodology to achieve filter polarization independence, which we validated using filters designed for the telecom O-band on a 400-nm-thick silicon nitride platform. By adjusting the grating dimensions to match the transmittances for both polarizations, we achieved a wavelength detuning between TE and TM polarizations of less than 0.3 nm. To validate this concept, we fabricated single-band, dual-band, and four-band filters, each with 3-nm notch bandwidth and 9-nm spacing. Experimental results closely match simulations, with only slight deviations in notch width and depth, which we attribute to variations in waveguide thickness and width. The fabricated filters exhibited notch rejections exceeding 25 dB and insertion loss of less than 1 dB for up to four-band transmittances. We believe that our design methodology is highly adaptable and can be applied to create polarization-agnostic integrated optical filters with arbitrary rejection spectra on platforms with similar index contrast, such as those based on polymers or lithium niobate. The proposed technique can also be extended to DWDM filters with narrower and more tightly spaced rejection bands. Preliminary calculations indicate that a dual-band grating operating at the C-band, with a spacing of 800 pm, notch width of 600 pm, and a rejection greater than 20 dB, exhibits a polarization wavelength detuning below 15% of the band spacing, at the expense of increased length (≈2.5 mm).

Supporting Information

Supporting Information is available from the Wiley Online Library or from the author.

Acknowledgements

Collaborative Science, Technology and Innovation Program (CSTIP) Small Teams (ST-R2-01-02) and High Throughput and Secure Networks Challenge Program at the National Research Council Canada (HTSN-210); Ministerio de Ciencia, Innovación y Universidades (FPU21/04914); and Ministerio de Economía y Competitividad (PDC2023-145833-I00, PID2023-151178OB-I00). Funding for open access charge: Universidad de Málaga/CBUA.

Conflict of Interest

The authors declare no conflict of interest.

Data Availability Statement

The data that support the findings of this study are available from the corresponding author upon reasonable request.

Keywords

integrated Bragg gratings, integrated optical filters, silicon photonics, silicon nitride, polarization independence

Received: December 5, 2024
Revised: April 8, 2025
Published online:

[1] N. Margalit, C. Xiang, S. M. Bowers, A. Bjorlin, R. Blum, J. E. Bowers, *Appl. Phys. Lett.* **2021**, *118*, 220501.
[2] D. Dai, D. Liang, P. Cheben, *Photonics Res.* **2022**, *10*, NGSP1.
[3] D. J. Blumenthal, R. Heideman, D. Geuzebroek, A. Leinse, C. Roeloffzen, *Proc. IEEE* **2018**, *106*, 2209.
[4] C. Xiang, W. Jin, J. E. Bowers, *Photonics Res.* **2022**, *10*, A82.
[5] J. C. Adcock, J. Bao, Y. Chi, X. Chen, D. Bacco, Q. Gong, L. K. Oxenløwe, J. Wang, Y. Ding, *IEEE J. Sel. Top. Quantum Electron.* **2021**, *27*, 1.
[6] A. Z. Subramanian, E. Ryckeboer, A. Dhakal, F. Peyskens, A. Malik, B. Kuyken, H. Zhao, S. Pathak, A. Ruocco, A. D. Groote, P. Wuytens, D. Martens, F. Leo, W. Xie, U. D. Dave, M. Muneeb, P. V. Dorpe, J. V. Campenhout, W. Bogaerts, P. Bienstman, N. L. Thomas, D. V. Thourhout, Z. Hens, G. Roelkens, R. Baets, *Photonics Res.* **2015**, *3*, B47.
[7] G. Gao, D. Chen, S. Tao, Y. Zhang, S. Zhu, X. Xiao, J. Xia, *Opt. Express* **2017**, *25*, 12260.
[8] Q. Wilmart, H. El Dirani, N. Tyler, D. Fowler, S. Malhouitre, S. Garcia, M. Casale, S. Kerdiles, K. Hassan, C. Monat, X. Letartre, A. Kamel, M. Pu, K. Yvind, L. K. Oxenløwe, W. Rabaud, C. Sciancalepore, B. Szelag, S. Olivier, *Appl. Sci.* **2019**, *9*, 255.
[9] Y. Li, Y. Zhang, L. Zhang, A. W. Poon, *Photonics Res.* **2015**, *3*, B10.
[10] D. Dai, L. Liu, S. Gao, D.-X. Xu, S. He, *Laser Photonics Rev.* **2013**, *7*, 303.
[11] Y. Wang, S. Bhat, N. Tessema, R. Kraemer, A. Napoli, G. Delrosso, N. Calabretta, *J. Light. Technol.* **2022**, *40*, 3432.
[12] Y. Peng, S. Hooten, Y. Yuan, Z. Huang, S. Cheung, W. V. Sorin, D. Liang, M. Fiorentino, R. G. Beausoleil, in 2024 IEEE Silicon Photonics Conf. SiPhotonics, IEEE, Tokyo Bay, Japan, **2024**, pp. 1–2.
[13] Y. Wu, X. Liu, T. Chu, *J. Light. Technol.* **2024**, *42*, 7307.
[14] J. Xue, J. Wu, C. Cheng, W. Zhang, B. Wang, Opt. Fiber Commun. Conf. (OFC), San Diego, California, USA, **2024**, pp. 1–3.
[15] X. Yi, D. Sun, W. Zhao, H. Li, L. Zhang, Y. Shi, D. Dai, *Nanophotonics* **2024**, *13*, 4149.
[16] M. Kohli, D. Chelladurai, B. Vukovic, D. Moor, D. Bisang, K. Keller, A. Messner, T. Buriakova, M. Zervas, Y. Fedoryshyn, U. Koch, J. Leuthold, *ACS Photonics* **2023**, *10*, 3366.

[17] A. Caut, V. Shekhawat, V. Torres-Company, M. Karlsson, *IEEE Photonics J.* **2024**, *16*, 1.
[18] M. Zhu, D. Liu, W. Li, W. Zhao, S. Zhao, C. Gao, J. He, Y. Peng, D. Dai, *J. Light. Technol.* **2024**, *42*, 2917.
[19] A. D. Simard, S. LaRochelle, *Opt. Express* **2015**, *23*, 16662.
[20] J. Wang, L. R. Chen, *Opt. Express* **2015**, *23*, 26450.
[21] D. Charron, W. Shi, in 2019 *Conf. Lasers Electro-Opt.* CLEO, **2019**, pp. 1–2.
[22] A. Fernández-Hinestrosa, J. M. Luque-González, P. Cheben, J. H. Schmid, S. Wang, J. G. Wangüemert-Pérez, I. Molina-Fernández, A. Ortega-Moñux, *Sci. Rep.* **2024**, *14*, 18492.
[23] J. Skaar, L. Wang, T. Erdogan, *IEEE J. Quantum Electron.* **2001**, *37*, 165.
[24] D. Pereira-Martín, J. M. Luque-González, J. G. Wangüemert-Pérez, A. Hadij-ElHouati, Í. Molina-Fernández, P. Cheben, J. H. Schmid, S. Wang, W. N. Ye, J. Čtyroký, A. Ortega-Moñux, *Opt. Express* **2021**, *29*, 15867.
[25] D. Dai, S. He, *IEEE Photonics Technol. Lett.* **2006**, *18*, 2017.
[26] C. Pérez-Armenta, A. Ortega-Moñux, J. M. Luque-González, R. Halir, P. J. Reyes-Iglesias, J. Schmid, P. Cheben, Í. Molina-Fernández, J. G. Wangüemert-Pérez, *Photonics Res.* **2022**, *10*, A57.
[27] E. Durán-Valdeiglesias, S. Guerber, D. Oser, X. L. Roux, D. Benedikovic, D. Pérez-Galacho, N. Vulliet, S. Cremer, S. Monfray, E. Cassan, D. Marris-Morini, C. Baudot, F. Boeuf, L. Vivien, C. Alonso-Ramos, *Opt. Lett.* **2019**, *44*, 4578.
[28] H. Yun, L. Chrostowski, N. A. F. Jaeger, *Opt. Lett.* **2019**, *44*, 847.
[29] N. Ning, H. Yu, Q. Zhang, Q. Huang, Z. Fu, P. Xia, Z. Wei, X. Wang, Y. Wang, J. Yang, *Opt. Lett.* **2023**, *48*, 65.
[30] D. Liu, D. Dai, *Opt. Express* **2019**, *27*, 20704.
[31] M. J. Strain, S. Thoms, D. S. MacIntyre, M. Sorel, *Opt. Lett.* **2014**, *39*, 413.
[32] S. Paul, T. Saastamoinen, S. Honkanen, M. Roussey, M. Kuittinen, *Opt. Lett.* **2017**, *42*, 4635.
[33] D. T. H. Tan, K. Ikeda, Y. Fainman, *Opt. Lett.* **2009**, *34*, 1357.
[34] J. Čtyroký, J. G. Wangüemert-Pérez, P. Kwiecien, I. Richter, J. Litvik, J. H. Schmid, Í. Molina-Fernández, A. Ortega-Moñux, M. Dado, P. Cheben, *Opt. Express* **2018**, *26*, 179.
[35] P. Cheben, J. Čtyroký, J. H. Schmid, S. Wang, J. Lapointe, J. G. Wangüemert-Pérez, Í. Molina-Fernández, A. Ortega-Moñux, R. Halir, D. Melati, D. Xu, S. Janz, M. Dado, *Opt. Lett.* **2019**, *44*, 1043.
[36] IEEE 802.3bs (**2017**). IEEE Standard for Ethernet - Amendment 10: Media Access Control Parameters, Physical Layers, and Management Parameters for 200 Gb/s and 400 Gb/s Operation. Institute of Electrical and Electronic Engineers.
[37] FS United Kingdom, "Gasping the Basic Knowledge of LAN-WDM (LWDM)," can be found under https://www.fs.com/uk/blog/gasping-the-basic-knowledge-of-lan-wdmlwdm-10915.html, **2024**(accessed: July 2025).
[38] C.-L. Chen, in *Foundations for Guided Wave Optics*, John Wiley & Sons, Inc., **2007**, pp. 169–205.
[39] J. Hong, W. Huang, T. Makino, *J. Light. Technol.* **1992**, *1*, 1860.
[40] Applied Nanotools Inc., "Silicon Nitride Design Rules and Area," can be found under https://www.appliednt.com/nanosoi/sys/resources/rules_nitride/, **2024** (accessed: July 2025).